Modeling of Grain Shape Effect on Multiaxial Plasticity of Metallic Polycrystals

Akrum Abdul-Latif

Modeling of Grain Shape Effect on Multiaxial Plasticity of Metallic Polycrystals

A. Abdul-Latif

Laboratoire d'Ingénierie des Systèmes Mécaniques et des Matériaux (LISMMA), Supméca,
3 rue Fernand Hainaut, 93407 Saint Ouen Cedex, France
e-mail: aabdul@iu2t.univ-paris8.fr

A simplified nonincremental interaction law is used describing the nonlinear elastic-inelastic behavior of FCC polycrystals proposed recently (Abdul-Latif and Radi, 2010, "Modeling of the Grain Shape Effect on the Elastic-Inelastic Behavior of Polycrystals with Self-Consistent Scheme," ASME J. Eng. Mater. Technol., 132(1), p. 011008). In this scheme, the elastic strain defined at the granular level based on the Eshelby's tensor is assumed to be isotropic, uniform and compressible. Hence, the approach considers that the inclusion (grain) has an ellipsoidal shape of half axes defining by a, b and c such as $a \neq b = c$. The granular heterogeneous inelastic strain is locally determined using the slip theory. Both elastic and inelastic granular strains depend on the granular aspect ratio ($\alpha = a/b$). An aggregate of grains of ellipsoidal shape is supposed to be randomly distributed with a distribution of aspect ratios having a log-normal statistical function. The effect of this distribution on the mechanical behavior is investigated. A host of cyclic inelastic behavior of polycrystalline metals is predicted under uniaxial and multiaxial loading paths. Using the aluminum alloy 2024, an original complex cyclic loading path type is proposed and carried out experimentally. After the model parameters calibration, the elastic-inelastic cyclic behavior of this alloy is quantitatively described by the model. As a conclusion, the model can successfully describe the elasto-inelastic at the overall and local levels.

Keywords: self-consistent model, ellipsoidal inclusion, cyclic elasto-inelastic behavior, aluminum alloy 2024, new biaxial cyclic test

1 Introduction

It is well-known that the majority of the machine components in-service are generally subjected to various complex cyclic loading paths leading to many experimental and theoretical investigations. Such studies focus on the cyclic behavior of materials under either strain- or stress-controlled conditions. Since the last decade, a large number of models have been developed to describe the cyclic behavior of materials for different problems. These studies show that such a behavior is generally sensitive to the complexity of the loading paths due to metallurgical changes at highly stressed or deformed regions. They particularly observe that nonproportional cyclic loading situations promoting often additional hardening of the material ([1–8], and many others).

In the nonproportional cyclic loading, the recorded additional hardening compared to that induced by proportional one is generally attributed to the slip system multiplication. This means that the cyclic hardening behavior appears to be strongly dependent on the applied loading path.

From a theoretical point of view, this additional-hardening phenomenon can be modeled either using classical macroscopic phenomenological approach (e.g., [3,9–13]), or employing the micromechanical (micro-macro) approach such as self-consistent methods (for example, [1,14–21]). The particular aspect which should be emphasized is that the macroscopic phenomenological approach requires often more constitutive equations and more material parameters. Therefore, for a reliable prediction with a large domain of validity (loading, temperature, environmental conditions) for a given material, experimental databases become so important that it may be practically impossible to be conducted since their realization is too hard and tedious. However, this is not the case for the micromechanical approach.

Moreover, several approaches have been proposed describing the material behavior based on the well-known dislocation dynamics concept simulating in both two and three spatial dimensions [22–25]. This concept can take into account multiple dislocations and the formation of dislocation substructures demonstrating successfully many of the essential features of strain aging and dislocation pinning (i.e., obstacle bypass mechanisms) in the presence of both mobile and immobile obstacles. The concept of dislocation dynamics can highlight the role of climb mobility in dislocation/obstacle interactions which occur when the dislocations motion has a component perpendicular to their slip plane with the existence of point defects and their long-range diffusion. Having an important effect on dislocation morphology, dislocation climb becomes important in high temperature creep. It is worth emphasizing that this approach is beyond the framework of the development presented in this paper. Indeed, the adopted theoretical concept is based on a self-consistent approach and not the dislocation dynamics.

Recently, the ellipsoidal inclusion case in the nonincremental interaction law already developed in [26] is used showing the impact of the grain shape on the cyclic elasto-inelastic behavior of polycrystals with the small strain assumption. In this study, this model will be presented with its simplified nonincremental interaction law using the log-normal distribution function of the granular aspect ratio. The model capability will be investigated describing the elastic-inelastic cyclic behavior of polycrystalline metallic materials under different loading situations (simple and complex) as a particular interest in this work. The obtained results show that this model faithfully reproduces the cyclic hardening. In fact, special emphasis is laid to the biaxial cyclic loading paths notably the nonproportional ones showing the additional hardening phenomenon in the case of aluminum alloy 2024. Hence, quantitative predictions of the elastic-inelastic cyclic behavior for

[1]Corresponding author.

the alloy are performed. The calibrated material parameters are validated by a new biaxial cyclic loading test (noted henceforth Tri-type). Finally, it is concluded that the overall predicted responses are in good agreement with the available experimental results.

2 Micromechanical Model

2.1 General Scope. In the used model, it is assumed that the ellipsoidal inclusion is embedded in infinite homogeneous matrix having a compressible, uniform and isotropic elasticity. The inelastic behavior is defined through the slip theory; assuming that the slip is the dominant deformation mechanism neglecting other mechanisms like twinning, grain boundaries sliding, etc. Only the intragranular isotropic hardening is introduced as an internal state variable at the crystallographic slip system (CSS). For more detailed information, the reader can be referred to the original paper [26]. The model uses the framework of the micromechanical theory of time-dependent plasticity with the small strain hypothesis. The simplified nonincremental interaction law of softened nature is considered to describe the nonlinear elastic-inelastic behavior of polycrystals. The effect of overall kinematic hardening on the overall polycrystal behavior is described naturally and implicitly via the simplified interaction law.

The ellipsoidal inclusion is defined by its aspect ratio α ($\alpha = a/b$ where a and b are the half-axes of the grain). In this work, the concept of the log-normal distribution function of α is considered, i.e., each grain within the aggregate has its own aspect ratio with an overall mean value of 1. This is reasonable since the engineering metallic materials have (or considered to have) an isotropic elasticity. This is due the fact that their grains have a near-equiaxed shape.

Grains within the aggregate are supposed to have different orientations defined by its three well-known Euler angles with different aspect ratios α. Two microstructural scales are defined namely the mesoscale (grain) and the microscale (CSS) as the lowest one.

Throughout this paper, the index $s \in \{1, 2, \ldots, n\}$ is associated to the system rank, with n being the maximum number of octahedral systems in the grain ($n = 12$ for FCC). The index $g \in \{1, 2, 3, \ldots, N_g\}$ describes the grain rank with N_g being the maximum number of grains contained in the aggregate.

2.2 Choice of State Variables. The mechanical state of each level is supposed to be described by the following state variables:

- At the macroscale (grains aggregate): There are no state variables at this level. The overall stress tensor $\underline{\Sigma}$ (respectively, the overall strain tensor $\underline{E}$) being simple averages of the granular stress tensor $\underline{\sigma}^g$ (respectively, granular strain tensor $\underline{\varepsilon}^g$) are supposed to be homogeneous at this level.
- At the mesoscale (grain): the granular elastic tensor $\underline{\underline{\varepsilon}}^g_e$ is introduced as an internal state variable associated with the internal granular stress tensor $\underline{\sigma}^g$.
- At the microscale (CSS): a couple of internal state variables (q^s, R^s) represents the intragranular isotropic hardening; the dual scalar variable R^s is the thermodynamic force associated with the isotropic hardening variable q^s. These variables describe the expansion of the elastic domain on the slip system *s*.

All the grains within the aggregate are considered to have the same elastic coefficients. The overall elastic strain tensor $\underline{E}^e$ together with the overall inelastic strain tensor $\underline{E}^{in}$ are determined by using the localization-homogenization method [27].

2.3 Interaction Law. The interaction law of the polycrystalline structure is devoted to define the relations between the variables in each grain of the aggregate and the global variables. When a macroscopic stress tensor $\underline{\Sigma}$ is applied to the macroscale, then the granular stress tensor $\underline{\sigma}^g$ is determined using the simplified nonincremental interaction law of ellipsoidal inclusion [26]:

$$\underbrace{\left(\underline{\underline{\Im}}^{s^{-1}} + \underline{\underline{C}}\right)^{-1} : (\dot{\underline{\sigma}}^g - \dot{\underline{\Sigma}})}_{\text{1st term}} + \underbrace{\Gamma\left(\underline{\underline{\Im}}''^{-1} + \underline{\underline{A}}'\right)^{-1} : (\underline{s}^g - \underline{S})}_{\text{2nd term}} = (\dot{\underline{\varepsilon}}^g - \dot{\underline{E}}) \tag{1}$$

where

$$\left[\underline{\underline{A}}\right] = \Gamma\left[\underline{\underline{A}}'\right]$$

and

$$\left[\underline{\underline{\Im}}'\right] = \frac{1}{\eta}\left[\underline{\underline{\Im}}''\right]$$

with $\underline{\underline{A}}$ is the macroscopic 4th order tangent modulus tensor and $\underline{\underline{\Im}}'$ being the inelastic interaction tensor. The ratio $(1/\eta)$ is replaced by a phenomenological viscous parameter considered as a new model parameter, independent on the strain history ($\Gamma > 0$) together with the use of the classical hookean elasticity to prevent the problem of η adjustment for satisfying the self-consistency conditions and for accelerating the computing time. $\underline{\underline{\Im}}^s$ and $\underline{\underline{\Im}}'$ are 4th order tensors which should be determined using $\underline{\underline{A}}$ and $\underline{\underline{C}}$ with Green function and integral methods, respectively. $\underline{\underline{C}}$ is the global stiffness tensor. $\dot{\underline{\varepsilon}}^g$ and $\dot{\underline{E}}$ are, respectively, the total granular and total overall strain rates. $\underline{s}^g$ and $\underline{S}$ are the granular and global deviatoric Cauchy stress tensors, respectively.

Note that the first term in Ref. [26] represents the elastic part, while the second one describes the viscoplastic behavior, where $\dot{\underline{\Sigma}} = \underline{\underline{C}} : \dot{\underline{E}}^e$ is the constitutive relation of global elasticity (hookean relation), and $\underline{S} = \underline{\underline{A}} : \dot{\underline{E}}^{in}$ represents the constitutive equation of global inelastic behavior.

The symmetrical Eshelby's tensor of elasticity $\underline{\underline{\Im}}^s$ for an isotropic behavior is expressed as follows:

$$[\Im^S_{ijkl}] = \begin{bmatrix} \Im^S_{iiii} & \Im^S_{iijj} & \Im^S_{iijj} & 0 & 0 & 0 \\ \Im^S_{iijj} & \Im^S_{iiii} & \Im^S_{iijj} & 0 & 0 & 0 \\ \Im^S_{iijj} & \Im^S_{iijj} & \Im^S_{iiii} & 0 & 0 & 0 \\ 0 & 0 & 0 & \Im^S_{ijij} & 0 & 0 \\ 0 & 0 & 0 & 0 & \Im^S_{ijij} & 0 \\ 0 & 0 & 0 & 0 & 0 & \Im^S_{ijij} \end{bmatrix} \tag{2a}$$

with

$$\Im^s_{iiii} = \frac{4\pi a^2 c}{15\mu(3\lambda^I + 6\mu^I)}\left[(\lambda^I + \mu^I + Q^{(1)}_{IK})(3\lambda^I + 2\mu^I) + \left(\frac{Q^{(1)}_{IK}}{2} - 3\lambda^I - 8\mu^I\right)(\lambda^I + 4\mu^I)\right] \tag{2b}$$

$$\Im^s_{iijj} = \frac{4\pi a^2 c}{15\mu(3\lambda^I + 6\mu^I)}\left[(\lambda^I + \mu^I + Q^{(1)}_{IK})(3\lambda^I + 2\mu^I) + 2\lambda^I\left(\frac{Q^{(1)}_{IK}}{2} - 3\lambda^I - 8\mu^I\right)\right] \tag{2c}$$

$$\Im^s_{ijij} = \frac{8\pi a^2 c}{15\mu(3\lambda^I + 6\mu^I)}\left[\frac{Q^{(1)}_{IK}}{2} - 3\lambda^I - 8\mu^I\right] \tag{2d}$$

where a, b, and c are the half axes of the ellipsoidal inclusion and λ^{I} and μ^{I} are its Lame's coefficients. By using the same approach as in Ref. [28], we have therefore: $Q_{IK}^{(1)} = Q_{11}^{(1)} + 2(Q_{12}^{(1)} + Q_{21}^{(1)}) + 4Q_{22}^{(1)}$ (see Appendix).

The isotropic elasticity tensor $\underline{\underline{C}}$, placed in infinite homogeneous matrix under macroscopic loading, is classically expressed by

$$C_{ijkl} = \lambda\delta_{ij}\delta_{kl} + \mu(\delta_{ik}\delta_{jl} + \delta_{il}\delta_{jk}) \tag{3}$$

According to Molinari et al. [29], the 4th order inelastic interaction tensor $\underline{\underline{\Im}}'$ is defined by

$$\Im'_{ijkl} = \frac{1}{4}(P_{ijkl} + P_{jikl} + P_{ijlk} + P_{jilk}) \tag{4}$$

Using Green's tensor technique, the 4th order tensor P_{ijkl} is then defined by

$$P_{ijkl} = \frac{-1}{4\pi}\int_0^{\pi} \sin\theta \left(\int_0^{2\pi} \psi_{jr} K_r \psi_{ks} K_s G_{il}(K)\, d\varphi \right) d\theta \tag{5}$$

where $[\psi]$ is the transformation matrix of spherical coordinates in elliptic coordinates, defined by

$$[\psi] = \begin{bmatrix} 1 & 0 & 0 \\ 0 & \frac{a}{b} & 0 \\ 0 & 0 & \frac{a}{c} \end{bmatrix} \tag{6}$$

and

$$K : \begin{cases} K_1 = k\sin\theta\cos\varphi \\ K_2 = \frac{a}{b}k\sin\theta\sin\varphi \\ K_3 = \frac{a}{c}k\cos\theta \end{cases}; \quad \text{with} \quad \begin{cases} 0 \le \theta \le \pi \\ 0 \le \varphi \le 2\pi \\ 0 \le k \le 1 \end{cases} \tag{7}$$

$$G_{il} = \left(\frac{2}{\eta k^2}\delta_{il} - \frac{2}{\eta k^4} K_i K_l \right) \tag{8}$$

where η is the coefficient of viscosity.

The symmetrical fourth order inelastic interaction tensor $\underline{\underline{\Im}}'$ with its coefficients can be therefore defined by

$$[\Im'_{ijkl}] = \frac{1}{\eta}\begin{bmatrix} \Im''_{1111} & \Im''_{1122} & \Im''_{1133} & 0 & 0 & 0 \\ \Im''_{2211} & \Im''_{2222} & \Im''_{2233} & 0 & 0 & 0 \\ \Im''_{3311} & \Im''_{3322} & \Im''_{3333} & 0 & 0 & 0 \\ 0 & 0 & 0 & \Im''_{2323} & 0 & 0 \\ 0 & 0 & 0 & 0 & \Im''_{1313} & 0 \\ 0 & 0 & 0 & 0 & 0 & \Im''_{1212} \end{bmatrix} \tag{9}$$

with

$$\Im''_{1111} = \frac{-4}{15} \tag{9a}$$

$$\Im''_{2222} = -\frac{2}{15}\left(5 - 3\left(\frac{a}{b}\right)^2\right)\left(\frac{a}{b}\right)^2 \tag{9b}$$

$$\Im''_{3333} = \frac{-2}{15}\left(5 - 3\left(\frac{c}{a}\right)^2\right) \tag{9c}$$

$$\Im''_{1212} = \frac{1}{30}\left(\frac{a^2(b-4a)(b+6a)}{b^4} - 5\right) \tag{9d}$$

$$\Im''_{1313} = \frac{1}{30}\left(\frac{c^2+2ac}{a^2} - 9\right) \tag{9e}$$

$$\Im''_{2323} = \frac{1}{30}\left(\frac{a}{b}\right)^2\left[\frac{(b+c)^2-5a^2}{b^2}\right] - 5\Bigg) \tag{9f}$$

$$\Im''_{1122} = \frac{2}{15}\frac{a^3}{b^3} \tag{9g}$$

$$\Im''_{1133} = \frac{2}{15}\frac{c}{a} \tag{9h}$$

$$\Im''_{2233} = \frac{2}{15}\frac{a^2 c}{b^3} \tag{9i}$$

The tangent modulus is deduced by its general matrix form

$$A'_{ijkl} = \eta\begin{bmatrix} A'_{1111} & A'_{1122} & A'_{1133} & 0 & 0 & 0 \\ A'_{2211} & A'_{2222} & A'_{2233} & 0 & 0 & 0 \\ A'_{3311} & A'_{3322} & A'_{3333} & 0 & 0 & 0 \\ 0 & 0 & 0 & A'_{2323} & 0 & 0 \\ 0 & 0 & 0 & 0 & A'_{1313} & 0 \\ 0 & 0 & 0 & 0 & 0 & A'_{1212} \end{bmatrix} \tag{10a}$$

The coefficients of the tangent modulus are [30]

$$A'_{1111} = \frac{4}{3}\left[(\zeta-1)\frac{\dot{E}^{in}_{11}\dot{E}^{in}_{11}}{(\dot{p}^{eq})^2} + 1\right] \tag{10b}$$

$$A'_{2222} = \frac{4}{3}\left[(\zeta-1)\frac{\dot{E}^{in}_{22}\dot{E}^{in}_{22}}{(\dot{p}^{eq})^2} + 1\right] \tag{10c}$$

$$A'_{3333} = \frac{4}{3}\left[(\zeta-1)\frac{\dot{E}^{in}_{33}\dot{E}^{in}_{33}}{(\dot{p}^{eq})^2} + 1\right] \tag{10d}$$

$$A'_{1122} = \frac{2}{3}\left[2(\zeta-1)\frac{\dot{E}^{in}_{11}\dot{E}^{in}_{22}}{(\dot{p}^{eq})^2} - 1\right] \tag{10e}$$

$$A'_{1133} = \frac{2}{3}\left[2(\zeta-1)\frac{\dot{E}^{in}_{11}\dot{E}^{in}_{33}}{(\dot{p}^{eq})^2} - 1\right] \tag{10f}$$

$$A'_{2233} = \frac{2}{3}\left[2(\zeta-1)\frac{\dot{E}^{in}_{22}\dot{E}^{in}_{33}}{(\dot{p}^{eq})^2} - 1\right] \tag{10g}$$

$$A'_{1212} = \frac{2}{3}\left[2(\zeta-1)\frac{\dot{E}^{in}_{12}\dot{E}^{in}_{12}}{(\dot{p}^{eq})^2} + \frac{3}{2}\right] \tag{10h}$$

$$A'_{1313} = \frac{2}{3}\left[2(\zeta-1)\frac{\dot{E}^{in}_{13}\dot{E}^{in}_{13}}{(\dot{p}^{eq})^2} + \frac{3}{2}\right] \tag{10i}$$

$$A'_{2332} = \frac{2}{3}\left[2(\zeta-1)\frac{\dot{E}^{in}_{23}\dot{E}^{in}_{23}}{(\dot{p}^{eq})^2} + \frac{3}{2}\right] \tag{10j}$$

where $\dot{E}^{in}_{ij}$ is the overall inelastic strain rate tensor, ζ is the strain rate sensitivity parameter, $\dot{p}^{eq}$ is the overall equivalent plastic strain rate given by

$$\dot{p}^{eq} = \sqrt{\frac{2}{3}\dot{E}^{in}_{ij}\dot{E}^{in}_{ij}} \tag{11}$$

The resolved shear stresses τ^s at the CSS scale are defined by the resistance to dislocation motion due to the presence of microstructural inhomogeneities. They are obtained, after determining the stress tensor at each grain $\underline{\sigma}^g$ employing the interaction law [26],

by the twice-contracted tensorial product between $\underline{\sigma}^{g}$ and the Schmid factor matrix (2nd order orientation tensor) $\underline{m}^{s}$:

$$\tau^{s} = \underline{\sigma}^{g} : \underline{m}^{s} \tag{12a}$$

$$\underline{m}^{s} = \frac{1}{2}\left(l_{i}^{s} e_{j}^{s} + l_{j}^{s} e_{i}^{s}\right) \tag{12b}$$

where $\mathbf{e}^{s}$ is the unit vector in the slip direction and $\mathbf{l}^{s}$ is the unit vector normal to the slip plane.

The determination of τ^{s} together with the intragranular isotropic hardening (q^{s}, R^{s}) on each CSS gives the actual slip rate $\dot{\gamma}^{s}$ from which the granular inelastic strain rate $\underline{\dot{\varepsilon}}_{in}^{g}$ can be defined. Finally, the overall inelastic strain rate $\underline{\dot{E}}^{in}$ can be deduced by the homogenization of $\underline{\dot{\varepsilon}}_{in}^{g}$.

2.4 State Potential. The state of the system is described by its free energy (state potential). The granular free energy is considered as the sum of the reversible and irreversible energies per unit volume under small strain and isothermal conditions. The granular elastic and inelastic parts of specific free energy ψ^{g} can be written as

$$\rho\psi^{g}(\underline{\varepsilon}_{e}^{g}, q^{s}) = \rho\psi_{e}^{g}(\underline{\varepsilon}_{e}^{g}) + \rho\psi_{in}^{g}(q^{s}) \tag{13}$$

where ρ is the granular material density.

Based on the assumption of the isotropic elasticity, the granular free energy per unit volume is expressed as a classical isotropic quadratic function of the granular elastic strain tensor $\underline{\varepsilon}_{e}^{g}$ given by

$$\rho\psi_{e}^{g}(\underline{\varepsilon}_{e}^{g}) = \frac{1}{2}\lambda^{I}(\mathrm{tr}\underline{\varepsilon}_{e}^{g})^{2} + \mu^{I}\mathrm{tr}(\underline{\varepsilon}_{e}^{g})^{2} \tag{14}$$

Thermodynamically, its associated variable (granular stress tensor $\underline{\sigma}^{g}$) is defined by

$$\underline{\sigma}^{g} = \rho\frac{\partial\psi_{e}^{g}}{\partial\underline{\varepsilon}_{e}^{g}} = 2\mu^{I}\underline{\varepsilon}_{e}^{g} + \lambda^{I}(\mathrm{tr}\underline{\varepsilon}_{e}^{g})\underline{1} \tag{15}$$

In the isothermal case, it is assumed that the granular elasticity coefficients (λ^{I} and μ^{I}) remain always constants. Thus, the time derivative of Eq. (15) gives

$$\dot{\underline{\sigma}}^{g} = 2\mu^{I}\dot{\underline{\varepsilon}}_{e}^{g} + \lambda^{I}(\mathrm{tr}\dot{\underline{\varepsilon}}_{e}^{g})\underline{1} \tag{16}$$

where $\underline{1}$ is the 2nd order unit tensor.

According to the small strain hypothesis, the total granular strain $\underline{\varepsilon}^{g}$ is partitioned into elastic $\underline{\varepsilon}_{e}^{g}$ and inelastic $\underline{\varepsilon}_{in}^{g}$ part:

$$\underline{\varepsilon}^{g} = \underline{\varepsilon}_{e}^{g} + \underline{\varepsilon}_{in}^{g} \tag{17}$$

The granular inelastic part of the state potential $\rho\psi_{in}^{g}(q^{s})$ is formulated as a quadratic function of the internal state variable q^{s}:

$$\rho\psi_{in}^{g} = \frac{Q}{2}\sum_{r=1}^{n}\sum_{s=1}^{n} H_{rs} q^{r} q^{s} \tag{18}$$

where Q is the intragranular isotropic hardening modulus of a given CSS. It is assumed, for simplicity, that all the slip systems have the same hardening modulus. For FCC the polycrystals, the hardening interaction matrix H_{rs} is of 12×12 describing dislocation-dislocation interaction allowing the introduction of the cross influence of the slip of the system *s* on the hardening of the system *r*, belonging to the same family or not. The dual variable R^{s} (state law) can be derived from Eq. (18) as follows:

$$R^{s} = \rho\frac{\partial\psi_{in}^{g}}{\partial q^{s}} = Q\sum_{r=1}^{n} H_{rs} q^{r} \tag{19}$$

This hardening tends to saturate on each slip system depending on the amount of the slip on the same system (self-hardening) as well as on the other slip systems within the same grain (cross hardening).

2.5 Dissipation Analysis: Complementary Relations. The basic goal of the dissipation analysis is to deduce the evolution equations associated with the dissipative phenomena. After determining the associated force R^{s}, the formulation should be completed by the rate equations of $\dot{q}^{s}$. The determination of the local inelastic flow is conducted by adopting a threshold concept. Hence, the evolution rates can be obtained by introduction of a yield surface for each slip system f^{s} as well as dissipation potential F^{s} considering the nonassociated plasticity case. Note that the nonlinearity of the intragranular isotropic hardening is introduced by the inelastic potential F^{s}. Before giving these complementary relations (evolution equations), it is important to underline that the yield surface is considered at the CSS level using the Schmid type convex of microplasticity depending on the resolved shear stress τ^{s} together with the hardening

$$f^{s} = |\tau^{s}| - R^{s} - k_{o}^{s} \tag{20}$$

where k_{o}^{s} is the initial critical resolved shear stress. Hence, a system can be activated when the absolute value of its resolved shear stress τ^{s} is greater than the actual flow surface radius ($R^{s} + k_{o}^{s}$). The slip rate can be determined as long as the stress and the hardening variables are known.

In the framework of this approach, the rate of change of the isotropic hardening variable ($\dot{q}^{s}$) can be derived from the following intragranular inelastic dissipation potential F^{s} for each system:

$$F^{s} = f^{s} + b^{s} q^{s} R^{s} \tag{21}$$

where b^{s} is material coefficient characterizing the nonlinearity of the local isotropic hardening

The evolution laws of the granular inelastic strain and the isotropic hardening variables are deduced by the generalized normality rule:

At the granular level

$$\dot{\underline{\varepsilon}}_{in}^{g} = \sum_{s=1}^{n}\dot{\lambda}^{s}\frac{\partial F^{s}}{\partial\underline{\sigma}^{g}} = \sum_{s=1}^{n}\dot{\lambda}^{s}\mathrm{sign}(\tau^{s})\,\underline{m}^{s} = \sum_{s=1}^{n}\dot{\gamma}^{s}\,\underline{m}^{s} \tag{22}$$

$$\text{with} \quad \dot{\gamma}^{s} = \dot{\lambda}^{s}\mathrm{sign}(\tau^{s}) \tag{23}$$

where $\dot{\gamma}^{s}$ is the slip rate on the slip system.

It is obvious that the slip theory is adapted to describe the inelastic behavior. However, the uniformity of the plastic strain concept within a grain is one of the theoretical hypotheses related to the interaction law [26]. Despite this theoretical remark, impressive capacities of several self-consistent research programs are obtained (e.g., [16,19,24,26,31,32]) where the principal cyclic hardening phenomena are faithfully described. Therefore, we consider that the present approach is a pragmatic solution justified by the quality of recorded predictions.

At the CSS level, the rate of the isotropic hardening variable is expressed by

$$\dot{q}^{s} = -\sum_{r=1}^{n}\dot{\lambda}^{r}\frac{\partial F^{r}}{\partial R^{s}} = \dot{\lambda}^{s}(1 - b^{s} q^{s}) \tag{24}$$

By using the viscoplasticity concept, the value of pseudomultiplier $\dot{\lambda}^{s}$ for each slip system occurring along closed-packed crystallographic slip planes and directions is a power function of the distance to the yield point defined by the criterion f^{s}:

$$\dot{\lambda}^s = \left(\frac{f^s}{K^s}\right)^{z^s} = \left(\frac{|\tau^s| - R^s - k_o^s}{K^s}\right)^{z^s} \tag{25}$$

where K^s and z^s are material constants describing the local viscous effect of the material.

Since the rate independent models (considering that plastic flow at the slip system level is a rate independent), do not possess the uniqueness in the numerical applications, the rate dependent slip is therefore considered to resolve such numerical difficulties used previously by several researchers. Although, the developed model is a rate dependent type, the rate independent case can be practically obtained by choosing a high value of viscous exponent z^s and a low value of the coefficient K^s, i.e., by minimizing the viscosity effect.

At the macroscale, the transition from the single to polycrystal response is performed by the well-known averaging procedures depending on the granular elastic and inelastic rates. It is worth noting that, for homogenous elastic media, it has been demonstrated [33–35] that the overall stresses $\underline{\Sigma}$ (respectively, the overall strain $\underline{E}^e$) is the simple average of the granular stresses $\underline{\sigma}^g$ (respectively, granular strains $\underline{\varepsilon}_e^g$). This is not the case for the overall inelastic strain where the averaging procedure is usually not simple but involves localization tensors [36,37]. Nevertheless, in the case of elasto-inelastic behavior of homogeneous elasticity, the overall inelastic strain $\underline{\dot{E}}^{in}$ can be defined as an average of the granular inelastic deformations $\underline{\dot{\varepsilon}}_{in}^g$ [35]. In the single-phase polycrystal with isotropic elasticity case, the overall elastic and inelastic strain rates are equal to the average of granular rates $\underline{\dot{\varepsilon}}_e^g$ and $\underline{\dot{\varepsilon}}_{in}^g$ [36]. Thus, the rates of change of the overall elastic and inelastic strains are calculated, respectively, as follows:

$$\underline{\dot{E}}^e = \sum_{g=1}^{Ng} v^g \underline{\dot{\varepsilon}}_e^g \tag{26}$$

$$\underline{\dot{E}}^{in} = \sum_{g=1}^{Ng} v^g \underline{\dot{\varepsilon}}_{in}^g \tag{27}$$

where v^g is the volume fraction of the same oriented grains.

The overall total strain is given by

$$\underline{\dot{E}} = \underline{\dot{E}}^e + \underline{\dot{E}}^{in} \tag{28}$$

2.6 Positivity of the Intrinsic Dissipation. The intrinsic dissipation at the granular level is given by

$$\underline{\sigma}^g : \underline{\dot{\varepsilon}}_{in}^g - \sum_{s=1}^{n} R^s \dot{q}^s \geq 0 \tag{29}$$

By using Refs. [18], [19], [21], and [22], it is easy to show the thermodynamical admissibility of the single-crystal. This can be made showing that the inequality [29] is satisfied as long as the parameters Q^s and k_o^s are positive.

2.7 Grain Shape Distribution Function. The grain shape distribution in heterogeneous polycrystals which provides local heterogeneity can be characterized by several experimental techniques. In this work, the volume fraction of individual grain shape is a key parameter since it has an important impact on the mechanical behavior and represents also the reality in the polycrystalline metallic materials. Hence, an accurate description of grain shape via its aspect ratio α can lead to suitable local and global mechanical behaviors of polycrystals. Consequently, a log-normal distribution function of the variable α is determined in such a manner that the variable $x = \ln(\alpha)$ pursues a normal distribution. The probability density function is therefore defined by

$$p(\alpha) = \frac{1}{\alpha S\sqrt{2\pi}} \exp\left[-\frac{1}{2}\left(\frac{\ln(\alpha) - M}{S}\right)^2\right] \tag{30}$$

where M and S are the mean value and standard deviation of the variable x, respectively with

$$\int_0^\infty p(\alpha)d\alpha = 1$$

Different discrete log-normal distributions for a given mean and different dispersions are generated adopting the same procedure as given in previous works [38–40]. Since the metallic polycrystalline materials are always considered to have isotropic elastic behavior because their grains have a near-equiaxed shape. Therefore, Fig. 1 shows statistical volume weighted distributions for three different relative dispersions having the same mean aspect ratio of 1.

3 Experimental Program

As mentioned previously in Ref. [41], an experimental program has already been carried out on the well-known aluminum alloy 2024. It was carried out at room temperature on a servo-hydraulic INSTRON machine (type 1340), using thin-walled tubes (internal

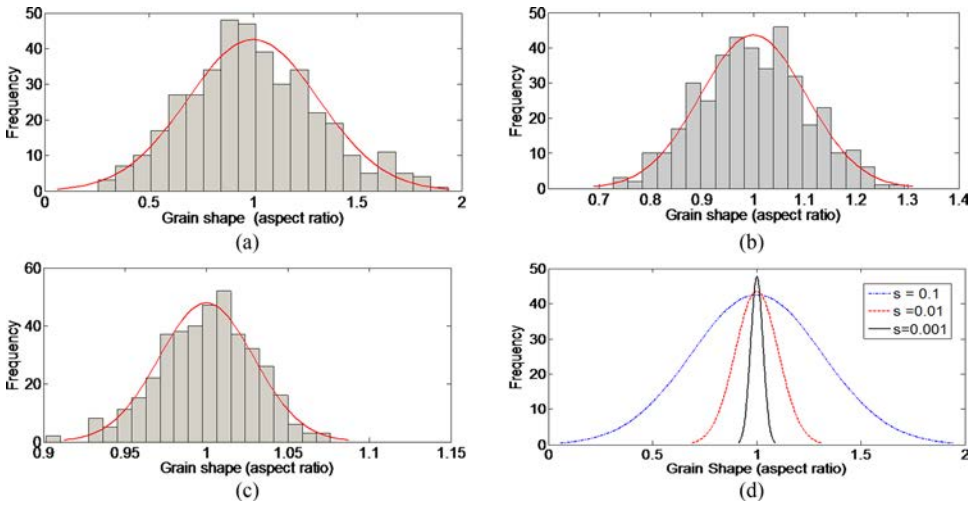

Fig. 1 Volume weighted grain-shape distribution determined with the mean aspect ratio of 1 with different standard deviations of: (*a*) S = 0.1, (*b*) S = 0.01, (*c*) S = 0.001

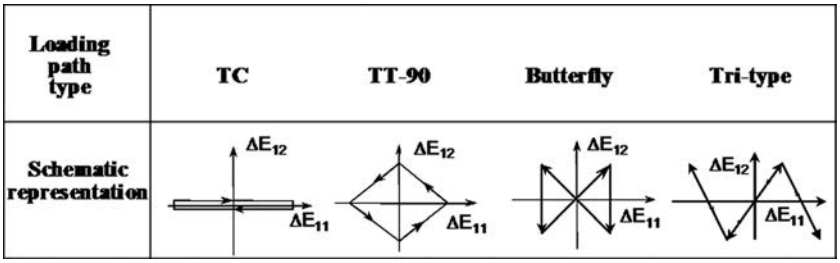

Fig. 2 Employed cyclic loading paths

diameter: 15 mm and external diameter: 18 mm). Several uniaxial and biaxial loading paths, with a triangle waveform, were conducted. The maximum von-Mises equivalent total strain is defined as follows:

$$\text{For uniaxial tension-compression test: } \varepsilon^{t}_{eq_{max}} = \frac{\varepsilon_{max} - \varepsilon_{min}}{2}$$

$$\text{For biaxial tension-torsion test: } \varepsilon^{t}_{eq_{max}} = \max\left(\sqrt{\varepsilon^2 + \frac{\gamma^2}{3}}\right)$$

Where ε is the overall normal strain and γ is the overall shear strain.

After machining process, all specimens undergo an over-aging heat treatment. This treatment consists of a setting the specimens in solution with 495 °C, followed by a water quench.

In this work, beside the several cyclic tests carried out previously, an original cyclic test is conducted in this study. Indeed, it is a special loading type noted "Tri-type." It consists of imposing strain amplitudes according to 11 (ΔE_{11}) and 12 (ΔE_{12}) directions (Fig. 2). There are for a period of tension-compression (one cycle), three torsion-torsion cycles. The other used tests are schematically illustrated in Fig. 2 which are: uniaxial tension-compression (noted TC), biaxial tension-torsion with 90 deg out-of-phase angle (TT90) and butterfly test (Fly). Note that all these tests are made under strain-controlled condition having the same Mises equivalent strain of $\varepsilon^{t}_{eq_{max}} = 0.85\%$.

TC test has been conducted under a total strain-controlled condition of $\Delta\varepsilon_{11} = 1.7\%$ with a period of 20 s. Moreover, the TT90 biaxial loading path has been conducted using a couple of values: $\Delta\varepsilon_{11} = 1.47\%$ and $\Delta\gamma_{12} = 1.48\%$ having a period of 40 s. Under the butterfly test, the imposed strains are: $\Delta\varepsilon_{11} = 1.47\%$ and $\Delta\gamma_{12} = 1.47\%$. The period of the axial strain is 100 s and that of shear one is 50 s. As far as the new Tri-type test is concerned, two strain values of $\Delta\varepsilon_{11} = 1.46\%$ and $\Delta\gamma_{12} = 1.48\%$ are controlled having 150 s for the axial strain and 50 s for the shear one. In this test, cyclic hardening effect is obviously observed through the hysteresis loops. In the tension-compression phase (i.e., 11 direction) with a strain amplitude of $\Delta\varepsilon_{11}$ of 1.46% (Fig. 3(a)), one can clearly notice the presence of both hardening types (isotropic and kinematic). Furthermore, in the 12 direction phase with an amplitude of shear strain of $\Delta\varepsilon_{12} = 0.74\%$, the cyclic hardening is also clearly illustrated in Fig. 3(b). It is important to emphasize that an atypical behavior is captured. In fact, two families of hysteresis loops are recorded with an overlapping zone between them. Moreover, each family shows its cyclic hardening with a symmetrical manner with respect to each other. As a material response, Fig. 3(c) shows the hysteresis loops related to the overall stress-stress space ($\Sigma_{11} - \Sigma_{12}$) and its hardening evolutions with an almost symmetrical behavior in tension-compression and in torsion-torsion during loading up to steady state.

4 Application to Aluminum Alloy 2024

4.1 Determination of the Model Constants. The constitutive equations of the model are programmed into a computer code. Experimental databases of uniaxial cyclic (TC) and biaxial (TT90 and Fly) of the alloy are employed to calibrate the model parameters. The identification of parameters is performed using an initially random crystal distribution of 400 grains. The

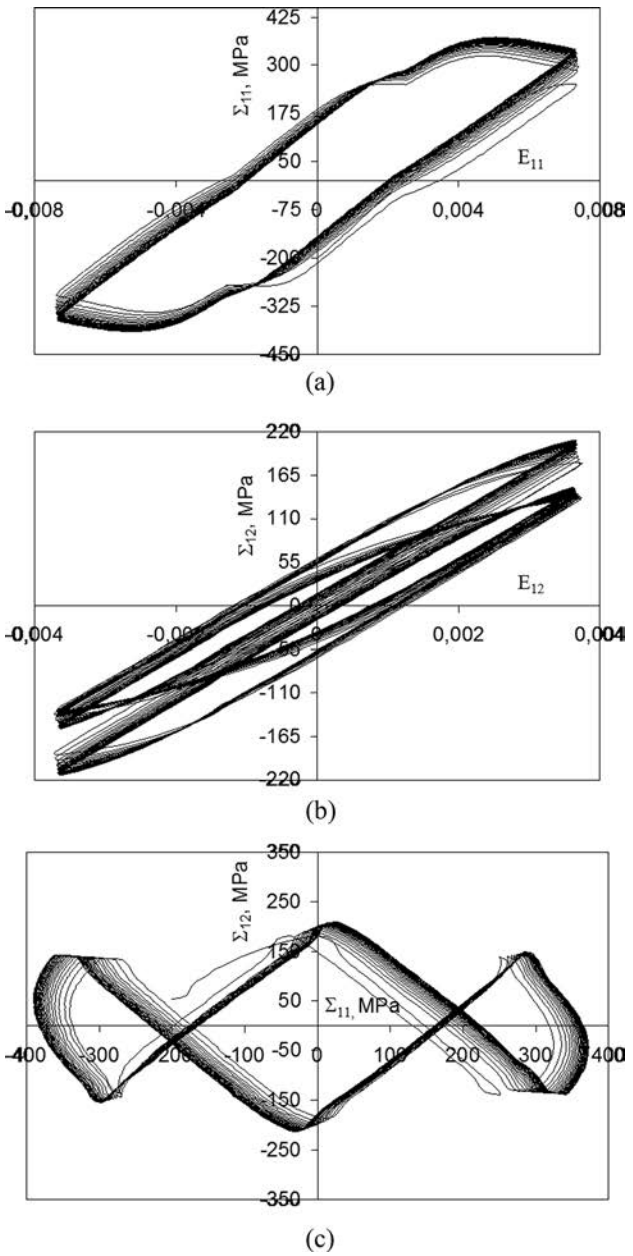

Fig. 3 Experimental curves of aluminum alloy 2024 (*a*): Σ_{11}-E_{11}, (*b*): Σ_{12}-E_{12} and (*c*): Σ_{11}-Σ_{12} for tri-type test up to cyclic stabilization

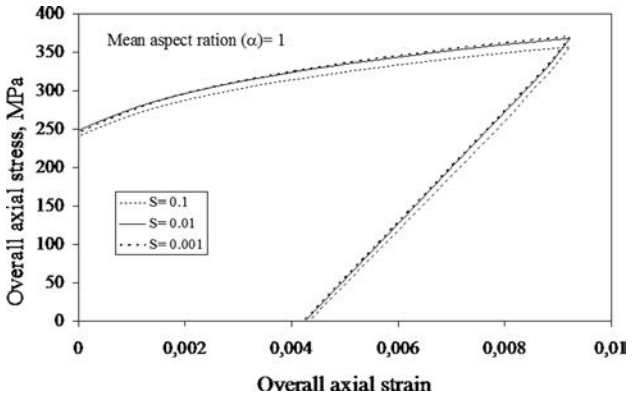

Fig. 4 Predicted uniaxial stress-strain for the cyclic steady state for different distributions of grain shape having different standard deviation of S = 0, 0.1, 0.01, and 0.001

microstructure of this aggregate (number and orientation of grains) is classically determined. In fact, for each grain, the well-known Euler angles define its orientation and its aspect ratio. Besides, the introduced orientations should suitably cover any space direction. This aggregate represents actually a reasonable compromise between minimizing the computing time and properly describing the polycrystalline microstructure. In order to ensure the macroscopic isotropy of the elastic behavior of this aggregate, it has been already shown in Ref. [42] that it fulfills the initial isotropic elastic behavior. Since the volume fraction of individual grain shape is a key parameter having a significant influence on the mechanical behavior description of polycrystalline metallic materials giving however the same overall mean aspect ratio of 1. Three different distributions of grain shape with three standard deviations of $S = 0.1$, 0.01, and 0.001 are simulated. Hence, Fig. 4 shows the predicted results for the stabilized cycle in TC for these three cases. In the identification and simulation process, the distribution of $S = 0.01$ is henceforth utilized for several reasons: first one is based on the computing time and the second is related to an accurate description of the grain shape which can lead to correct local and global mechanical behavior of polycrystals.

The computer code uses the well-known Runge–Kutta of 2nd order algorithm with adaptive step size. With a non stiff problem, this algorithm consists of improving the accuracy of the solution y (t). Its principle basis is the same as for the Euler method; whereas a difference is based on the introduction of additional correction terms to the iterative relation for reducing rounding errors. This approach is largely used for solving ordinary differential equations systems. It is a single-step method directly derived from the Euler method. It has the advantage of being easy to implement and stable for those functions used in physics.

To solve the model constitutive equations, these equations are presented as internal state variables: (1) Intragranular isotropic hardening variables q^s; (2) Viscoplastic pseudomultiplier λ^s for each crystallographic slip system; (3) Granular stress tensor $\underline{\sigma}^g$ obtained via the interaction law; (4) Granular elastic strain tensor $\underline{\varepsilon}_e^g$; (5) Granular inelastic strain tensor $\underline{\varepsilon}_{in}^g$; (6) Overall total strain tensor $\underline{E}$.

As a result, $\dot{\underline{Y}}$ is considered as a vector defined as follows:

$$\langle \dot{\underline{Y}} \rangle = \left\langle \dot{\underline{E}}, \dot{\underline{\sigma}}^g, \dot{\underline{\varepsilon}}_e^g, \dot{\underline{\varepsilon}}_{in}^g, \dot{\lambda}^s, \dot{q}^s \right\rangle$$

In this study, a FCC polycrystalline structure is considered. Hence, the number of scalar equations to be solved is $N_{eq} = 13 + 42 \times N_g$. The first number corresponds to $6 \times 2 + 1 = 13$ (components of elastic $\underline{E}_e$, inelastic $\underline{E}_{in}$ tensors and overall accumulated inelastic strain), $N_g \times 6 \times 3$ ($\underline{\sigma}^g$, $\underline{\varepsilon}_e^g$, and $\underline{\varepsilon}_{in}^g$ granular variables) as well as

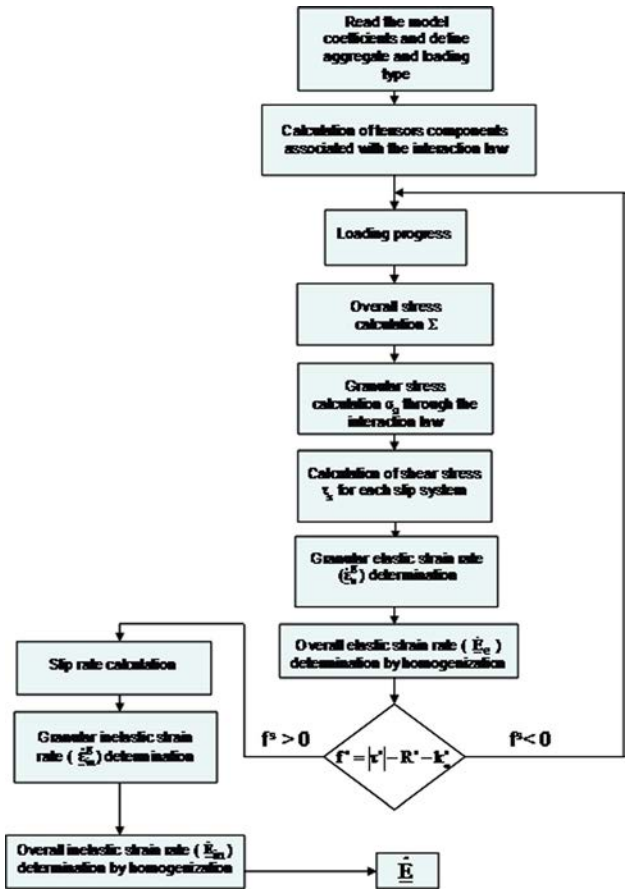

Fig. 5 Programming flow chart of the model

$N_g \times 12 \times 2$ ($\dot{\lambda}^s$ and $\dot{q}^s$ variables). The initial conditions are effectively assumed to be totally known ($\langle \underline{Y} \rangle_{t_n = t_0} = \langle \underline{Y}_0 \rangle$).

We consider therefore that at the instant $t_{n+1} = t_n + \Delta t$, an increment of total overall strain ΔE (or an increment of overall stress $\Delta\Sigma$ under stress-controlled condition) is applied to the grains aggregate. It is assumed that $\langle \underline{Y} \rangle_{t_n} = \left\langle \underline{E}, \underline{\sigma}^g, \underline{\varepsilon}_e^g, \underline{\varepsilon}_{in}^g, \lambda^s, q^s \right\rangle$ is known at the instant t_n, we then require to define how the most accurate space increments of the following variables and measurements

$\langle \Delta \underline{Y} \rangle = \left\langle \Delta \underline{E}, \Delta \underline{\sigma}^g, \Delta \underline{\varepsilon}_e^g, \Delta \underline{\varepsilon}_{in}^g, \Delta \lambda^s, \Delta q^s \right\rangle$ that allow to have for each time step, the solution $\langle \underline{Y} \rangle_{t_{n+1}}$ from the used algorithm as follows:

$$\langle \underline{Y} \rangle_{t_{n+1}} = \langle \underline{Y} \rangle_{t_n} + \langle \Delta \underline{Y} \rangle$$

Figure 5 shows the flow chart for the model programming.

There are ten material parameters which require identification. First, Young's modulus is directly determined using the experimental database and Poisson's ratio is initially defined by having an almost standard value of 0.3 for the metals. Then, it is assumed, for the sake of simplicity, that the overall elasticity constants λ and μ are thus equal to these of granular ones λ^I and μ^I, respectively, due to the isotropic elasticity assumption. All the grains have the same values of the λ^I and μ^I constants. Thus, they are computed from the overall Young's modulus and Poisson's ratio using the classical elasticity relations.

Although the model is a viscoplastic type, one can practically identify the plastic behavior by minimizing the viscosity effect. This can be made by choosing a high value of viscous exponent z^s and a low value of the coefficient K^s. The coefficients concerning the initial yield stress of the slip system k_o^s and the intragranular isotropic hardening (Q^s and b^s) should be also determined. Besides, there are six coefficients of the intragranular isotropic

Table 1 Employed values of the model constants

λ^I (MPa)	35590	Q (MPa)	945
μ^I (MPa)	28500	b^s	63
k^s_o (MPa)	45.4	Γ	2×10^{-6}
K^s	100	ζ	0.05
z^s	11.5	h_6	2.1

hardening matrix: h_1 is always equal to one (diagonal term) and $h_2, \ldots, h_6$ are nondiagonal terms. Indeed, based on some obtained results [41], it is considered that the values of $h_1 = h_2 = h_3 = h_4 = h_5 = 1$. So, only h_6 needs identification. On the other hand, to identify the model viscous parameter Γ, a detailed investigation has been already conducted [26,32]. It is initially defined using a value of 10^{-6}. The identified parameters for the employed alloy are used as initial values to begin the operation. Then, they are identified by conducting several iterations to minimize the deviation between the experimental and predicted results. Hence, the optimized material coefficients are specified as a best fit between the predicted and experimental results. The identified parameters are summed up in Table 1.

It is obvious that the correlated solutions are effectively in a good agreement with the experimental results (see Figs. 6(*a*), 6(*b*), and 6(*c*)). This is not surprising, since the experimental results of TC, TT90 and Fly are used in calibrating the model parameters. For the uniaxial and biaxial cyclic behavior of the employed alloy, the cyclic hardening evolutions together with the additional one (in the case of TT90 and Fly) are correctly represented by the model. Note that the predicted hardening evolution is always governed by the intragranular isotropic hardening

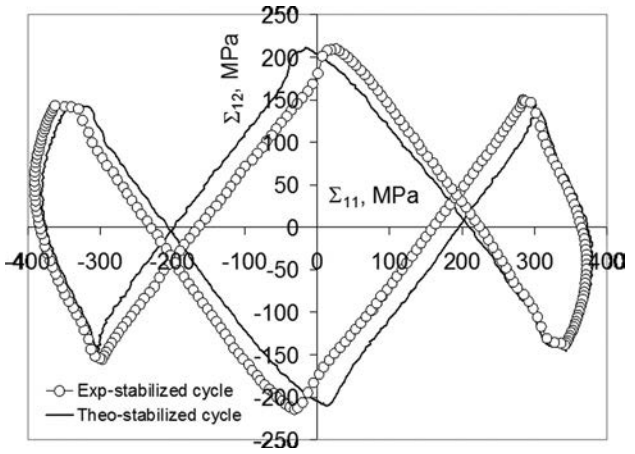

Fig. 7 Comparison between the experimental and predicted evolutions at steady-state for aluminum alloy 2024 under Tri-type loading path

determined at the CSS level and by the model parameter Γ. Hence, greater is the complexity of the loading path, greater becomes the additional hardening.

4.2 Validation. The experimental database of conducted Tri-type cyclic test is designed and used to validate the calibrated model parameters of the alloy. The cyclic hardening behavior especially the additional one is simulated by the model with the

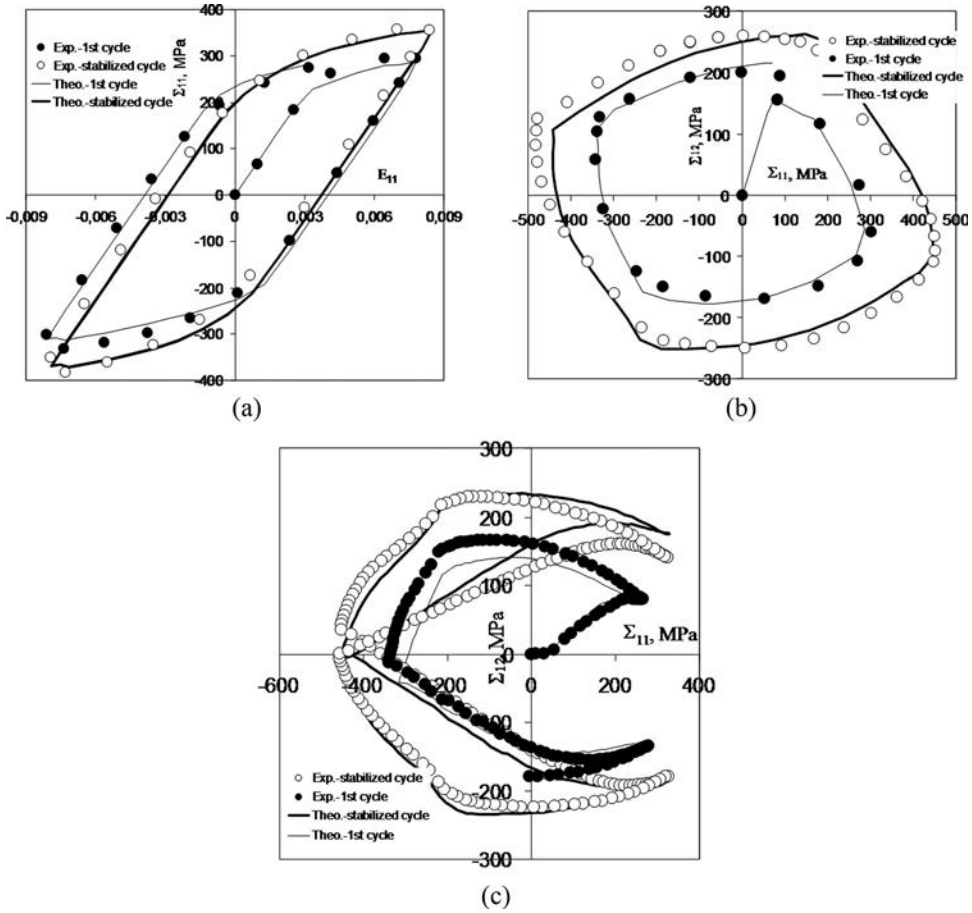

Fig. 6 Plots showing the correlation of the self-consistent model with corresponding experimental responses (first cycle and stabilized one) for aluminum alloy 2024 under different loading path complexity in: (*a*) TC, (*b*) TT90, and (*c*) butterfly

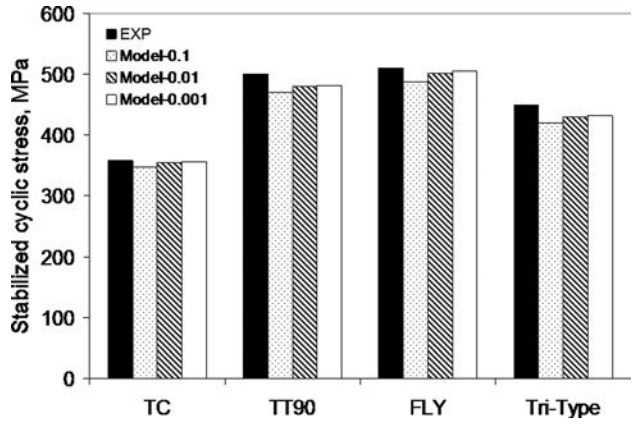

Fig. 8 Comparison between the experimental and predicted evolutions of the maximum von-Mises stress at steady-state for aluminum alloy 2024 under the four employed cyclic loading paths using for the simulations three distributions of grain shape with standard deviations of S = 0, 0.1, 0.01, and 0.001

already identified parameters. According to Fig. 7, the model is able to faithfully characterize the overall cyclic response particularly the additional hardening induced by this loading path. Furthermore, a careful examination of the data in Fig. 8 points out that the predicted overall maximum stabilized von-Mises stresses for the four used cyclic loadings using the comparison of the three distributions of aspect ratios α with standard deviations of $S = 0$, 0.1, 0.01, and 0.001. Through the histogram of this figure, it can be easily concluded that the model describes faithfully the additional hardening and its level due to the loading path complexity compared to the experimental results.

5 Concluding Remarks

With ellipsoidal grain shape consideration, a simplified self-consistent model proposed recently [26] is tested under several simple and complex cyclic loading conditions. The aggregate of grains is supposed to be randomly distributed with a distribution of aspect ratio based on a log-normal statistical function. The type of distribution displays its influence on the mechanical behavior of polycrystals. Also, it is shown that this model is capable to successfully describe the nonlinear overall cyclic hardening behavior of FCC polycrystals. This hardening evolution is always governed by the intragranular isotropic hardening determined at the crystallographic slip system level and by the model parameter Γ.

Induced by the complexity of loading path, the additional cyclic hardening is correctly reproduced by the model. In fact, greater is the complexity of the loading path, greater is the number of activated systems, greater becomes consequently the additional hardening. Identification and validation of materials parameters is performed using FCC polycrystalline aluminum alloy 2024. A new biaxial cyclic loading path of Tri-type is designed and then used for the validation of the model identified parameters. Based on several comparisons between the overall predicted responses and experimental results, it is obvious that the model is able to faithfully describe the mechanical cyclic behavior of the alloy under different complex cyclic loading paths.

Appendix

The integral calculation of both sides of the Green operator ($\underline{\underline{E}}$ and $\underline{\underline{F}}$) is given by:

$$\int_I \underline{\underline{\Gamma}}(\underline{x},\underline{x}')dV' = \int_I (\underline{\underline{E}}(x) + \underline{\underline{F}}(x - x'))dV' \tag{A1}$$

$$\int_I E_{ijkl}dV' = \frac{4\pi abc}{15\mu(3\lambda + 6\mu)}[(\lambda^I + \mu^I)\delta_{ij}\delta_{kl} - (3\lambda^I + 8\mu^I)I_{ijkl}] \tag{A2}$$

According to Ju and Sun [28], if x is outside the inclusion, Eshelby tensor is defined by:

$$\underline{\underline{G}}(x - x') = \int_I \underline{\underline{F}}(x - x')dV' = \frac{1}{4(1-\upsilon)} \times \begin{bmatrix} Q_{IK}^{(1)}(\lambda)\delta_{ij}\delta_{kl} + Q_{IJ}^{(2)}(\lambda)(\delta_{ik}\delta_{jl} + \delta_{il}\delta_{jk}) \\ + Q_I^{(3)}(\lambda)\delta_{ij}e_k e_l + Q_k^{(4)}(\lambda)\delta_{kl}e_i e_j \\ + Q_I^{(5)}(\lambda)(\delta_{ik}e_j e_l + \delta_{il}e_j e_k) \\ + Q_I^{(6)}(\lambda)(\delta_{jk}e_i e_l + \delta_{jl}e_i e_k) \\ + Q_{IJKL}^{(7)}(\lambda)e_i e_j e_k e_l \end{bmatrix} \tag{A3}$$

The components of $\underline{\underline{G}}$ are given by:

$$Q_{IK}^{(1)}(\lambda) = -2\upsilon J_I(\lambda) + \frac{a_I^2}{a_I^2 - a_K^2}J_I(\lambda) + \frac{a_k^2}{a_k^2 - a_I^2}J_k(\lambda) \tag{A4}$$

$$Q_{IJ}^{(2)}(\lambda) = -(1-\upsilon)[J_I(\lambda) + J_J(\lambda)] + \frac{a_I^2}{a_I^2 - a_J^2}J_I(\lambda) + \frac{a_J^2}{a_J^2 - a_I^2}J_J(\lambda) \tag{A5}$$

$$Q_I^{(3)}(\lambda) = 2\rho^3(\lambda)\left[1 - \rho_I^2(\lambda)\right] \tag{A6}$$

$$Q_k^{(4)}(\lambda) = 2\rho^3(\lambda)\left[1 - 2\upsilon - \rho_K^2(\lambda)\right] \tag{A7}$$

$$Q_I^{(5)}(\lambda) = 2\rho^3(\lambda)\left[\upsilon - \rho_I^2(\lambda)\right] \tag{A8}$$

$$Q_J^{(6)}(\lambda) = 2\rho^3(\lambda)\left[\upsilon - \rho_J^2(\lambda)\right] \tag{A9}$$

$$Q_{IJkl}^{(7)}(\lambda) = 2\rho^3(\lambda)\begin{bmatrix} 2\left(\rho_I^2(\lambda) + \rho_J^2(\lambda) + \rho_K^2(\lambda) + \rho_L^2(\lambda)\right) \\ + \rho_m(\lambda)\rho_m(\lambda) - \dfrac{4\rho_M^2(\lambda)\Theta_m(\lambda)\Theta_m(\lambda)}{\Theta(\lambda)} - 5 \end{bmatrix} \tag{A10}$$

where $\rho_I(\lambda)$, $\rho(\lambda)$, and $J_I(\lambda)$ are defined by:

$$\rho_I(\lambda) = \frac{a_I}{\sqrt{a_I^2 + \lambda}}, \quad \rho(\lambda) = [\rho_1(\lambda)\rho_2(\lambda)\rho_3(\lambda)]^{1/3},$$
$$J_I(\lambda) = \int \frac{\rho^3(\lambda)}{a_I^2 + \lambda}d\lambda$$

The integral calculation of Eq. (A3) is implicit for an ellipsoidal inclusion; thus, we take x inside the inclusion, with $\lambda = 0$, for a spheroid inclusion, Eq. (A3) becomes:

$$\int_I F_{ijkl}dV' = Q_{IK}^{(1)}\delta_{ij}\delta_{kl} + Q_{IJ}^{(2)}(\delta_{ik}\delta_{jl} + \delta_{il}\delta_{jk}) \tag{A11}$$

The coefficients of the two tensors $Q_{IK}^{(1)}$ and $Q_{IJ}^{(2)}$ are:

$$Q_{11}^{(1)} = \left[4\upsilon + \frac{2}{\alpha^2 - 1}\right]h(x) + 4\upsilon + \frac{4}{3(\alpha^2 - 1)} \tag{A12}$$

$$Q_{12}^{(1)} = Q_{13}^{(1)} = \left[4\upsilon - \frac{2\alpha^2 + 1}{\alpha^2 - 1}\right]h(x) + 4\upsilon - \frac{2\alpha^2}{\alpha^2 - 1} \tag{A13}$$

$$Q_{21}^{(1)} = Q_{31}^{(1)} = \left[-2\upsilon - \frac{2\alpha^2 + 1}{\alpha^2 - 1}\right]h(x) - \frac{2\alpha^2}{\alpha^2 - 1} \tag{A14}$$

$$Q_{22}^{(1)} = Q_{23}^{(1)} = Q_{32}^{(1)} = Q_{33}^{(1)} = \left[-2\upsilon + \frac{4\alpha^2 - 1}{4(\alpha^2 - 1)}\right] h(x) + \frac{\alpha^2}{2(\alpha^2 - 1)} \quad \text{(A15)}$$

and:

$$Q_{11}^{(2)} = \left[-4\upsilon + \frac{4\alpha^2 - 2}{\alpha^2 - 1}\right] h(x) - 4\upsilon + \frac{12\alpha^2 - 8}{3(\alpha^2 - 1)} \quad \text{(A16)}$$

$$Q_{12}^{(2)} = Q_{21}^{(2)} = Q_{13}^{(2)} = Q_{31}^{(2)} = \left[-\upsilon - \frac{\alpha^2 + 2}{\alpha^2 - 1}\right] h(x) - 2\upsilon - \frac{2}{\alpha^2 - 1} \quad \text{(A17)}$$

$$Q_{22}^{(2)} = Q_{23}^{(2)} = Q_{32}^{(2)} = Q_{33}^{(2)} = \left[2\upsilon - \frac{4\alpha^2 - 7}{4(\alpha^2 - 1)}\right] h(x) + \frac{\alpha^2}{2(\alpha^2 - 1)} \quad \text{(A18)}$$

where ν is the Poisson's ratio and h(x) is defined by:

$$h(x) = \begin{cases} -\dfrac{\alpha^2}{\alpha^2 - 1} + \dfrac{\alpha^2}{(\alpha^2 - 1)^{3/2}} \mathrm{Ln}\left[(\alpha^2 - 1)^{1/2} + \alpha\right], & \text{pour } \alpha > 1 \\ -\dfrac{\alpha^2}{\alpha^2 - 1} + \dfrac{\alpha}{(1 - \alpha^2)^{3/2}} \tan^{-1} \dfrac{\alpha}{(1 - \alpha^2)^{1/2}}, & \text{pour } \alpha < 1 \end{cases} \quad \text{(A19)}$$

where a, b, and c are the three semiaxes of the ellipsoid and λ^I and μ^I are Lame's coefficients of the inclusion. The fourth order identity tensor is defined by:

$$I_{ijkl} = \frac{1}{2}(\delta_{ik}\delta_{jl} + \delta_{il}\delta_{jk}) \quad \text{(A20)}$$

References

[1] Moosbrugger, J. C., and McDowell, D. L., 1989, "On a Class of Kinematic Hardening Rules for Nonproportional Cyclic Plasticity," ASME J. Eng. Mater. Technol., **111**, pp. 87–98.

[2] Doong, S. H., and Socie, D. F., 1991, "Constitutive Modeling of Metals Under Nonproportional Cyclic Loading," ASME J. Eng. Mater. Technol., **113**, pp. 23–30.

[3] Abdul-Latif, A., 1996, "Constitutive Equations for Cyclic Plasticity of Waspaloy," Int. J. Plasticity, **12**, pp. 967–985.

[4] Bocher, L., Delobelle, P., Robinet, P., and Feaugas, X., 2001, "Mechanical and Microstructural Investigations of an Austenitic Stainless Steel Under Non-Proportional Loadings in Tension–Torsion-Internal and External Pressure," Int. J. Plasticity, **17**, pp. 1491–1530.

[5] Yaguchi, M., and Takahashi Y., 2005, "Ratchetting of Viscoplastic Material With Cyclic Softening—Part 1: Experiments on Modified 9Cr–1Mo Steel," Int. J. Plasticity, **21**, pp. 43–65.

[6] Zhang, J., and Jiang, Y., 2005, "An Experimental Investigation on Cyclic Plastic Deformation and Substructures of Polycrystalline Copper," Int. J. Plasticity, **21**, pp. 2191–2211.

[7] Kang, G., Kan, Q., Zhang, J., and Sun, Y., 2006, "Time-Dependent Ratchetting Experiments of SS304 Stainless Steel," Int. J. Plasticity, **22**, pp. 858–894.

[8] Kang, G., 2008, "Ratchetting: Recent Progresses in Phenomenon Observation, Constitutive Modeling and Application," Int. J. Fatigue, **30**, pp. 1448–1472.

[9] McDowell, D. L., 1985, "A Tow Surface Model for Transient Nonproportional Cyclic Plasticity," ASME J. Appl. Mech., **52**, pp. 298–308.

[10] Benallal, A., and Marquis, D., 1987, "Constitutive Equations for Nonproportional Cyclic Elasto-Viscoplasticity," ASME J. Eng. Mater. Technol., **109**, pp. 326–336.

[11] Voyiadjis, G. Z., and Sivakumar, S. M., 1991, "A Robust Kinematic Hardening Rule for Cyclic Plasticity With Ratchetting Effects," Acta Mech., **90**, pp. 105–123.

[12] Zhang, Z., Delagnes, D., and Bernhart, G., 2002, "Anisothermal Cyclic Plasticity Modeling of Martensitic Steels," Int. J. Fatigue, **24**, pp. 635–648.

[13] Vanegas-Márquez, E., Mocellin, K., Toualbi, L., De Carlan, Y., and Logé, R. E., 2012, "A Simple Approach for the Modeling of an ODS Steel Mechanical Behavior in Pilgering Conditions," J. Nucl. Mater., **420**, pp. 479–490.

[14] Cailletaud, G., 1992, "A Micromechanical Approach to Inelastic Behaviour of Metals," Int. J. Plasticity, **8**, pp. 55–73.

[15] Hess, F., 1993, "Anisotropic Strain Hardening in Polycrystalline Copper and Aluminum," Int. J. Plasticity, **9**(4), pp. 405–420.

[16] Kouddane, R., Molinari, A., and Canova, G. R., 1993, "Self-Consistent Modeling of Heterogeneous Viscoelastic and Elasto-Viscoplastic Materials," *Large Plastic Deformations: Fundamentals and Applications to Metal Forming*, Vol. 91, C. Teodosiu, J. L. Raphanel, and F. Sidoroff, eds., A. A. Balkema Publishers, Rotterdam, The Netherlands, p. 121–141.

[17] Zouhal, N., Molinari, A., and Toth, L. S., 1996, "Elastic-Plastic Effects During Cyclic Loading as Predicted by Taylor-Lin Model of Polycrystal Elasto-viscoplasticity," Int. J. Plasticity, **12**, pp. 343–360.

[18] Abdul-Latif, A., Dingli, J-Ph., and Saanouni, K., 1998, "Modeling of Complex Cyclic Inelasticity in Heterogeneous Polycrystalline Microstructure," J. Mech. Mater., **30**, pp. 287–305.

[19] Dingli, J. P., Abdul-Latif, A., and Saanouni, K., 2000, "Predictions of the Complex Cyclic Behavior of Polycrystals Using a New Self-Consistent Modeling," Int. J. Plasticity, **16**, pp. 411–437.

[20] Manonukul, A., Dunne, F. P. E., Knowles, D., and Williams, S., 2005, "Multiaxial Creep and Cyclic Plasticity in Nickel-Base Superalloy C263," Int. J. Plasticity, **21**, pp. 1–20.

[21] Evrard, P., Aubin, V., Degallaix, S., and Kondo, D., 2008, "Formulation of a New Single Crystal Law for Modeling the Cyclic Softening," Mech. Res. Commun., **35**, pp. 589–594.

[22] Rudolph, P., Frank-Rotsch, Ch., Juda, U., and Kiessling, F.-M., 2005, "Scaling of Dislocation Cells in GaAs Crystals by Global Numeric Simulation and Their Restraints by In Situ Control of Stoichiometry," Mater. Sci. Eng., A, 400–401, pp. 170–174.

[23] Xiang, Y., and Srolovitz, D. J., 2006, "Dislocation Climb Effects on Particle Bypass Mechanisms," Philos. Mag., **86**, pp. 3937–3957.

[24] Chen, Z., Chu, K. T., Srolovitz, D. J., Rickman, J. M., and Haataja, M. P., 2010, "Dislocation Climb Strengthening in Systems With Immobile Obstacles: Three-Dimensional Level-Set Simulation Study," Phys. Rev. B, **81**, p. 054104.

[25] Bako, B., Clouet, E., Dupuy, L. M., and Blétry, M., 2011, "Dislocation Dynamics Simulations With Climb: Kinetics of Dislocation Loop Coarsening Controlled by Bulk Diffusion," Philos. Mag., **91**, pp. 3173–3191.

[26] Abdul-Latif, A., and M. Radi, 2010, "Modeling of the Grain Shape Effect on the Elastic-Inelastic Behavior of Polycrystals With Self-Consistent Scheme," ASME Eng. Mater. Technol., **132**(1), p. 011008.

[27] Germain, P., Nguyen, Q. S., and Suquet, P., 1983, "Continuum Thermodynamics," ASME J. Appl. Mech., **105**, pp. 1010–1020.

[28] Ju, J. W., and Sun, L. Z., 1999, "A Novel Formulation for the Exterior Point Eshelby's Tensor of an Ellipsoidal Inclusion," ASME J. Appl. Mech., **66**, pp. 570–574.

[29] Molinari, A., Canova, G. R., and Ahzi, S., 1987, "A Self-Consistent Approach of the Large Deformation Viscoplasticity," Acta Metall., **35**, pp. 2983–2994.

[30] Molinari, A., EL Houdaigui, F., and Toth, L. S., 2004, "Validation of Tangent Formulation for the Solution of the Non-Linear Eshelby Inclusion Problem," Int. J. Plasticity, **20**, pp. 291–307.

[31] Radi, M., and Abdul-Latif, A., 2009, "Grain Form Effect on the Biaxial Elasto-Inelastic Behavior of Polycrystals With a Self-Consistent Approach," Phys. Procedia, **1**, pp. 13–16.

[32] Radi, M., and Abdul-Latif, A., 2012, "A Self-Consistent Approach Describing the Strain Induced Anisotropy: Case of Yield Surface Evolution," Comput. Mater. Sci., **54**, pp. 356–369.

[33] Hill, R., 1966, "Generalized Constitutive Relations for Incremental Deformation of Metal Crystals by Multislip," J. Mech. Phys. Solids, **4**, pp. 95–102.

[34] Mandel, J., 1965, "Une Généralisation de la Théorie de la Plasticité de W. T. Koiter," Int. J. Solids Struct., **1**, pp. 273–295.

[35] Bui, H. D., 1969, "Étude de L'Évolution de la Frontière du Domaine Élastique avec L'écrouissage et Relations de Comportement Élastoplastique de Métaux Cubiques," Ph.D. thesis, Paris, France.

[36] Mandel, J., 1971, "Plasticité Classique et Viscoplasticité," *Cours CISM, Udine*, Vol. 97, Springer-Verlag, New York.

[37] Bui, H. D., Dang Van, K., and Stolz, C., 1982, "Relations Entre Grandeurs Microscopiques et Macroscopiques Pour un Solide Anélastique Ayant Des Zones Endommagées," C.R. Acad. Sci., Ser. IIc: Chim., **294**, pp. 1155–1158.

[38] Zhu, B., Asaro, R., and Krysl, P., 2006, "Effects of Grain Size Distribution on the Mechanical Response of Nanocrystalline Metals: Part II," Acta Mater., **54**, pp. 3307–3320.

[39] Berbenni, S., Favier V., and Berveiller, M., 2007, "Impact of the Grain Size Distribution on the Yield Stress of Heterogeneous Materials," Int. J. Plasticity, **23**, pp. 114–142.

[40] Ramtani, S., Bui, H. Q., and Dirras, G., 2009, "A Revisited Generalized Self-Consistent Polycrystal Model Following an Incremental Small Strain Formulation and Including Grain-Size Distribution Effect," Int. J. Eng. Sci., **47**, pp. 537–553.

[41] Abdul-Latif, A., and Chadli, M., 2007, "Modeling of the Heterogeneous Damage Evolution at the Granular Scale in Polycrystals Under Complex Cyclic Loadings," Int. J. Damage Mechanics, **16**, pp. 133–158.

[42] Abdul-Latif, A., 2004, "Pertinence of the Grains Aggregate Type on the Self-Consistent Model Response," Int. J. Solids Struct., **41**, pp. 305–322.